JACS
JOURNAL OF THE AMERICAN CHEMICAL SOCIETY

Article

pubs.acs.org/JACS

pH and Amphiphilic Structure Direct Supramolecular Behavior in Biofunctional Assemblies

Tyson J. Moyer,[†,‡,#] Joel A. Finbloom,[†,§,#] Feng Chen,[†,∥] Daniel J. Toft,[∥] Vincent L. Cryns,*[,⊥] and Samuel I. Stupp*[,†,‡,§,∥]

[†]Institute for BioNanotechnology in Medicine and [∥]Department of Medicine, Feinberg School of Medicine, Northwestern University, Chicago, Illinois 60611, United States

[‡]Department of Materials Science and Engineering and [§]Department of Chemistry, Northwestern University, Evanston, Illinois 60208, United States

[⊥]Department of Medicine, Carbone Cancer Center, University of Wisconsin School of Medicine and Public Health, Madison, Wisconsin 53705, United States

Supporting Information

ABSTRACT: Supramolecular self-assembly offers promising new ways to control nanostructure morphology and respond to external stimuli. A pH-sensitive self-assembled system was developed to both control nanostructure shape and respond to the acidic microenvironment of tumors using self-assembling peptide amphiphiles (PAs). By incorporating an oligo-histidine H_6 sequence, we developed two PAs that self-assembled into distinct morphologies on the nanoscale, either as nanofibers or spherical micelles, based on the incorporation of the aliphatic tail on the N-terminus or near the C-terminus, respectively. Both cylinder and sphere-forming PAs demonstrated reversible disassembly between pH 6.0 and 6.5 upon protonation of the histidine residues in acidic solutions. These PAs were then characterized and assessed for their potential to encapsulate hydrophobic chemotherapies. The H_6-based nanofiber assemblies encapsulated camptothecin (CPT) with up to 60% efficiency, a 7-fold increase in CPT encapsulation relative to spherical micelles. Additionally, pH-sensitive nanofibers showed improved tumor accumulation over both spherical micelles and nanofibers that did not change morphologies in acidic environments. We have demonstrated that the morphological transitions upon changes in pH of supramolecular nanostructures affect drug encapsulation and tumor accumulation. Our findings also suggest that these supramolecular events can be tuned by molecular design to improve the pharmacologic properties of nanomedicines.

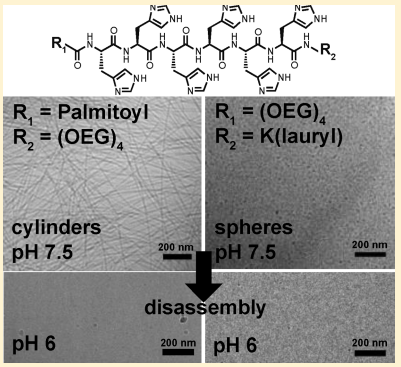

INTRODUCTION

Supramolecular self-assembly offers the potential to understand the role of noncovalent interactions in optimizing the delivery of therapeutics. Tailoring supramolecular interactions in a biological context is important for determining the ideal properties of a self-assembled drug carrier, such as size, shape, dynamics, and intermolecular cohesion.[1,2] Nanoscale drug carriers enable passive targeting of the tumor by taking advantage of the "enhanced permeability and retention" (EPR) effect,[3] which allows nanoparticles and macromolecules to diffuse mostly through the leaky vessels associated with tumors. The shape of the nanocarrier can further enhance tumor accumulation, with cylindrical morphologies exhibiting enhanced circulation times and efficacy over spherical particles.[4] Rod-like structures have also been shown to increase capacity to encapsulate drugs and to exhibit enhanced cellular uptake relative to spheres.[5−7]

In addition to the shape and size effects, the acidic environment present in much of the tumor parenchyma can induce molecular bond cleavage or nanostructure disassembly of a drug carrier through a selective pH trigger. Due to the high rate of glycolysis and production of lactic acid by tumor cells, the environment surrounding most tumors is more acidic than physiological pH (7.4), typically ranging from pH 5.5 to 7.[8−10] Through pH-sensitive delivery of chemotherapeutics, drugs can be released by conjugation of the drugs to nanocarriers via an acid-labile linker[8,11−13] or through the encapsulation of the drugs in a pH-dependent delivery system.[14−18] Additionally, nanostructures containing polyhistidine polymer segments (pK_a 6.5) have been shown to encapsulate drugs at physiological pH and exclusively release them at acidic pH.[14−18] Below pH 6.5, most of the histidine residues are protonated, causing electrostatic repulsion, which disrupts the nanostructures to release their cargo.

We report here on a pH-sensitive supramolecular system with histidine-based peptide amphiphiles. Peptide amphiphiles (PAs) are a unique class of self-assembling molecules with potential applications in regenerative medicine and other therapies, including cancer.[19−21] The nanofiber-forming PAs

Received: April 28, 2014
Published: October 13, 2014

   dx.doi.org/10.1021/ja5042429 | J. Am. Chem. Soc. 2014, 136, 14746−14752

developed in our laboratory are composed of β-sheet forming peptide segments conjugated to an aliphatic lipid tail, leading to assembly in aqueous media into high aspect ratio cylindrical fibers as a result of the combination of hydrophobic collapse and hydrogen bonding. PA assembly can be tuned through molecular design, including the choice of lipid tail and the nature of amino acids and their sequences in the β-sheet domain.[19,20,22−27] While recent efforts have been made to explore the pH-dependent assembly of PAs,[22,28] PAs that are sensitive to mildly acidic pH have not been evaluated for drug encapsulation or tumor accumulation. Additionally, PAs have been previously developed for cancer treatment by incorporating cytotoxic oligopeptide sequences into the PA backbone[19,29] and by encapsulating chemotherapeutic drugs.[21,30,31] We report here the synthesis of PAs that form either spherical or cylindrical supramolecular nanostructures and investigate their selective disassembly in acidic environments. We characterize the relationship between shape and pH dependence of disassembly in the context of tumor drug delivery.

EXPERIMENTAL SECTION

PA Synthesis. PAs were synthesized using fluorenylmethoxycarbonyl (Fmoc) solid-phase peptide synthesis and were purified as previously described.[30] All Fmoc-protected amino acids and Rink amide resin were purchased from Novabiochem, and 2-(1H-benzotriazole-1-yl)-1,1,3,3-tetramethyluronium hexafluorophosphate (HBTU) was purchased from P_3 Biosystems. 5,8,11,14-Tetraoxa-2-azahexadecanedioic acid (Fmoc-NH-OEG-CH_2COOH) was purchased from ChemPrep Inc. For the preparation of AlexaFluor 680 labeled PAs used in animal experiments, AF680-maleimide (Life Technologies) was reacted in PBS for 2 h with alternative versions of PAs **1**, **2**, and OEG-$K_2A_6K(C_{12})$, which incorporated a cysteine (C_{16}-H_6C-OEG, OEG-$CH_6K(C_{12})$ and the sequence OEG-$CK_2A_6K(C_{12})$, respectively). Following the reaction, samples were dialyzed overnight. Fluorescently labeled PAs were mixed in hexafluoroisopropanol (HFIP) with the original versions of PAs **1** and **2** and OEG-$K_2A_6K(C_{12})$, lyophilized, then dissolved in water, and lyophilized again to remove any residual HFIP. The final concentration of AF-680 PAs was 5 mol %, and fluorescence measurements were taken before injections at dilutions below the CACs to ensure equal dosing between groups.

Microscopy. Cryogenic transmission electron microscopy (cryo-TEM) was performed on a JEOL 1230 microscope with an accelerating voltage of 100 kV. Samples were prepared at 500 μM in PBS, and pH was adjusted with 1 M NaOH or 1 M HCl. Images were collected as described previously.[31]

Scattering Experiments. Small-angle X-ray scattering (SAXS) experiments were performed at the Advanced Photon Source, Argonne National Laboratory. The X-ray energy (15 keV) was selected using a double-crystal monochromator. The typical incident X-ray flux on the sample was $\sim 1 \times 10^{12}$ photons/s with a 0.2 × 0.3 mm^2 collimator. Liquid samples were dissolved in phosphate buffers with the desired pH at a concentration of 2.5 mM and were placed in 1.5 mm quartz capillary tubes and irradiated for 5 s. The 1D scattering profiles were obtained by azimuthal integration of the 2D patterns, with scattering from the capillaries subtracted as background. Scattering profiles were then plotted on a relative scale as a function of the scattering vector $q = (4\pi/\lambda)\sin(\theta/2)$, where θ is the scattering angle. For reversibility studies, solutions of 200 mM NaOH and 200 mM HCl were used to switch the pH between 6.0 and 7.5.

Circular Dichroism. Circular dichroism (CD) spectroscopy experiments were performed on a Jasco J-815 CD instrument courtesy of the Keck Biophysics Facility at Northwestern University. Samples were prepared at 250 μM in water. pH was adjusted using 1 M NaOH or 1 M HCl and measured with pH paper. An average of three trials were recorded for each sample.

Titrations. Titration studies were conducted by dissolving the PA in HCl (1 mM) for a final PA concentration of 1 mM. NaOH (20 mM) was then added in increments, and pH was measured with an electronic pH meter.

Critical Aggregation Concentration Studies. To determine the concentration at which the PA is able to encapsulate a hydrophobic molecule, critical aggregation concentration (CAC) studies were conducted with Nile Red dye (9-diethylamino-5-benzo[α]-phenoxazinone). Nile Red and PA were mixed together in PBS at an appropriate pH. The concentration of Nile Red was kept at 250 nM, while PA concentrations were varied. The maximum emission wavelengths (λ_{max}) were recorded for the Nile Red using a Nanolog fluorescence spectrophotometer. The maximum represents the average of three measurements, performed in duplicate experiments. In a hydrophobic environment, such as the one in the core of a PA assembly, the λ_{max} blue-shifted when compared to the emission in a hydrophilic environment.[32] The shifts in λ_{max} as a function of PA concentration were plotted, and the CAC values represented the lowest concentrations at which a redshift was observed.

Camptothecin Encapsulation and Release. Camptothecin (CPT) was encapsulated into PA nanofibers using a previously established encapsulation method.[30] Briefly, lyophilized PA was dissolved in HFIP (1,1,1,3,3,3-hexafluoro-2-propanol, 99.8+%, Sigma) and mixed together with CPT. The CPT concentration was held constant at 500 μM, while the PA:CPT ratio was varied from 10:1 to 0.31:1 using 2-fold dilutions of PA. The PA-CPT solution was sonicated for 30 min at 40 °C. After sonication, solutions were placed on a Schlenk line *in vacuo* for a minimum of 2 h to remove HFIP. The PA-CPT film was reconstituted to its original volume in PBS pH 7.0 and heated in a water bath for 30 min at 40 °C. Encapsulation efficiencies were measured by fluorescence (excitation/emission = 360/450 nm). Release studies were carried out as previously reported using specially built dialysis chambers.[31] The PA-CPT solutions were diluted 10-fold in PBS at appropriate pH, and release was measured after dialysis through a 3500 molecular weight cutoff membrane over 7 days. Due to low CPT solubility in PBS, release samples were diluted 1:100 in DMSO, and fluorescence was measured to determine release percent.

Cell Culture and Cell Viability Assay. MDA-MB 231 breast cancer cells were purchased from ATCC (Manassas, VA). Cell culture media and reagents were purchased from Invitrogen. 3-(4,5-Dimethylthiazol-2-yl)-5-(3-carboxymethoxyphenyl)-2-(4-sulfophenyl)-2H-tetrazolium (MTS)-cell viability assay reagents were purchased from Promega. Cells were cultured in high glucose DMEM containing 10% fetal bovine serum. Cells were plated in 96-well microtiter plates at 5000 cells per well and incubated for 2 h to allow for adherence. Where appropriate, pH 7.4 media was exchanged for pH 6.0 media adjusted with 1 M HCl to determine PA cytotoxicity at acidic pH. After 2 h, 10 μL of PA was added for the final appropriate concentrations. Cell viability was measured after 48 h using an MTS cell viability assay and was used according to the supplier's instructions. Briefly, the cell media was replaced after 48 h with a stock of 20% MTS solution in pH 7.4 media. The plate was incubated for 1−3 h, and absorbance was read using a Molecular Devices microplate reader (490 nm). Cell viability was calculated as an absorbance percent relative to the untreated cell control at the same pH. Experiments were performed in triplicate.

***In Vivo* Xenograft Tumor Experiments.** Mice were treated in accordance with the IACUC protocols at Northwestern University. Orthotopic xenograft tumors were established by intraductal injection of MDA-MB 231 breast cancer cells (1×10^6) into the mammary glands of female athymic nude mice (Harlan), and the tumors were allowed to grow for 4 weeks. Tail vein injections of 100 μL of labeled PAs were given at a concentration of 1.5 mM. Organs were imaged using IVIS fluorescent imaging at 645 ex/720 em, and fluorescence was quantified using the average radiant efficiency. Serum samples were obtained by tail vein bleeds at earlier time points (1, 6 h) and cardiac puncture at sacrifice (12, 24 h). Blood was spun down at 5000 g for 15 min, and the serum supernatant was then frozen until analyzed. Because the volume of blood extracted by tail vein bleeds is

dx.doi.org/10.1021/ja5042429 | J. Am. Chem. Soc. 2014, 136, 14746−14752

limited, 20 μL samples of serum were diluted 5× in PBS prior to quantification. Concentrations were determined using a standard curve of free AlexaFluor 680 dye. Measurements were performed using four mice per group.

RESULTS AND DISCUSSION

Materials Characterization of pH-Dependent Fibers. The PA molecules investigated here had peptide sequences containing six histidines (H_6), a hydrophobic tail, and a solubilizing oligo(ethylene glycol) (OEG) unit. To create a pH-sensitive cylindrical assembly, we synthesized a "forward" PA, PA **1**, containing an H_6 peptide sequence linked to palmitic acid at the N-terminus and the OEG group at the C-terminus (Figure 1A). The H_6 sequence comprises the pH-sensitive β-sheet forming region of the PA. We hypothesized that below pH 6.5, corresponding to the pK_a of histidine, the higher positive charge of the protonated histidines would disrupt the β-sheet hydrogen bonding necessary for fiber formation and lead to the disassembly of the PA fiber. PA **1** was characterized using cryo-TEM at pH 7.5 and 6.0 (Figure 1B,C). Cryo-TEM demonstrated the assembly of nanofibers at pH 7.5 into nanofibers and their subsequent disassembly at pH 6.0.

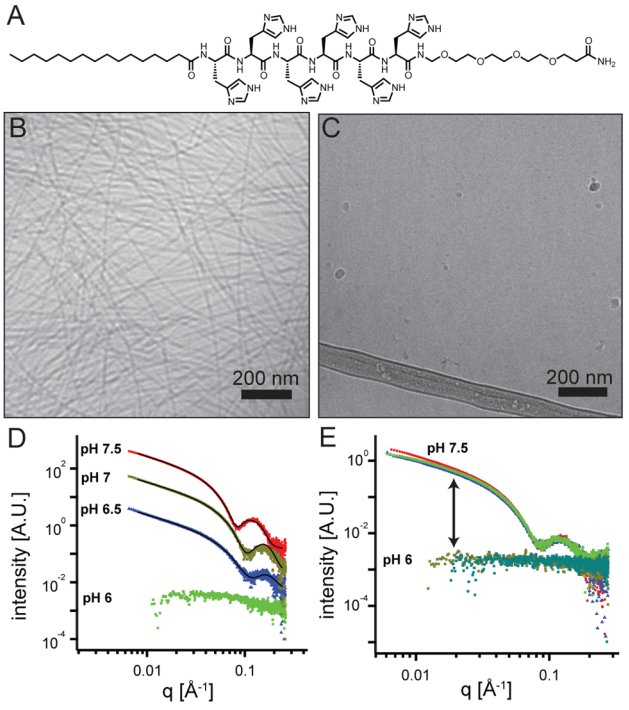

Figure 1. Characterization of $C_{16}H_6$–OEG PA **1**. (A) Structure of PA **1**. (B) Cryo-TEM of PA **1** at pH 7.5 and 500 μM. (C) Cryo-TEM of PA **1** at pH 6.0 and 500 μM. (D) SAXS of PA **1** at varying pH, with polydisperse core–shell cylinder models shown in black (intensities offset for clarity). (E) SAXS reversibility studies of PA **1**, where measurements of the same PA solution were taken immediately after each pH change. Each color represents a separate measurement.

To further analyze the supramolecular morphology of PA **1** in solution, SAXS was performed at varying values of pH, and the form factors were fit using cylindrical and spherical models to determine the supramolecular assembly morphology (Figure 1D). A polydisperse core–shell cylinder fit was performed for PA **1** at pH 7.5 and yielded a core radius of 1.4 nm and a shell thickness of 2.5 nm. Fitting of similar scattering patterns indicating cylindrical structures were observed at pH 6.5 and 7.0. The core radius remained constant at 1.4 nm, while the shell thickness decreased to 1.5 and 1.1 nm for pH 7.0 and 6.5, respectively. The reduction in fiber diameter could be the result of increased protonation of histidine residues toward the surface of the nanofiber. Once charged, the imidazole side chains are likely well solvated, changing the apparent thickness of the nanofiber shell by SAXS. At pH 6.0 a sharp drop in intensity was observed, and the scattering profile was the same as the solvent alone. A signature similar to that observed for PA **1** at pH 6.0 was previously reported for disassembled PA nanofibers,[31] suggesting that the 1D structures break up below pH 6.5. To determine the reversibility of this disassembly process, PA **1** was dissolved in PBS at pH 7.5, and the pH of the solution was adjusted back and forth three times from pH 7.5 to 6.0 using concentrated HCl and NaOH, and SAXS measurements were performed after each pH change (Figure 1E). The PA **1** solutions at pH 7.5 consistently showed nanofiber signatures by SAXS, while the scattering of the pH 6.0 solutions overlapped with the intensity of buffer alone. As suggested by SAXS measurements, PA **1** nanofibers undergo reversible assembly and disassembly processes.

The internal structure of PA **1** was further characterized with CD spectroscopy as a function of pH (Figure 1S). Previous studies have shown that PA nanofibers typically have β-sheet signatures with a minimum peak at 220 nm when analyzed by CD spectroscopy.[31,33] For PA **1**, β-sheet formation was observed at all pH values; however, at pH 6.0 the intensity of the 220 nm minimum decreased greatly as expected when the supramolecular structures disassembles as observed by SAXS and cryo-TEM. Titration studies of PA **1** (Figure 2S) displayed a pK_a of 5.5, which was below that of histidine and confirmed a transition in the protonation state of histidine residues in the pH range of the observed morphological changes. Lastly, the CAC of PA **1** was determined to be approximately 3 μM using Nile Red studies (Figure 3S). The λ_{max} of the Nile Red dye is blue-shifted when in a hydrophobic environment, such as the hydrophobic core of an assembled structure. By maintaining the Nile Red concentration at 250 nM and varying the concentration of the PA, we monitored the concentration at which the PA aggregated into a structure with a hydrophobic environment capable of encapsulating Nile Red. Shifts in λ_{max} were observed with PA **1** at both pH 7.5 and 6.0; however, the shift at pH 7.5 was more dramatic, corresponding to fiber formation at higher pH and suggesting a greater propensity for hydrophobic encapsulation than at pH 6.0. The hydrophobic nature of Nile Red could be inducing the formation of nanostructures, which would explain the differences when comparing the CAC measurements to cryo-TEM and SAXS at pH 6, carried out with PAs that did not contain hydrophobic cargo. Alternatively, cryo-TEM and SAXS may not be sensitive enough to detect a low concentration of nanostructures.

Characterization of pH-Dependent Spherical Micelles. A second PA was synthesized in which the functionalities of the C and N termini were switched to create a "reverse" PA. PA **2** (Figure 2A) retained the OEG and H_6 sequences; however, the OEG sequence was attached at the N-terminus, and lauric acid was conjugated to a lysine residue at the C-terminus to maintain a hydrophobic tail similar in length to the tail of PA **1**. PA **2** was characterized using the same methods as PA **1**. Surprisingly, the change in molecular design resulted in the self-assembly of spherical micelles at pH 7.5 as observed by cryo-TEM and SAXS (Figure 2B,D). The assembly into a spherical

dx.doi.org/10.1021/ja5042429 | J. Am. Chem. Soc. 2014, 136, 14746–14752

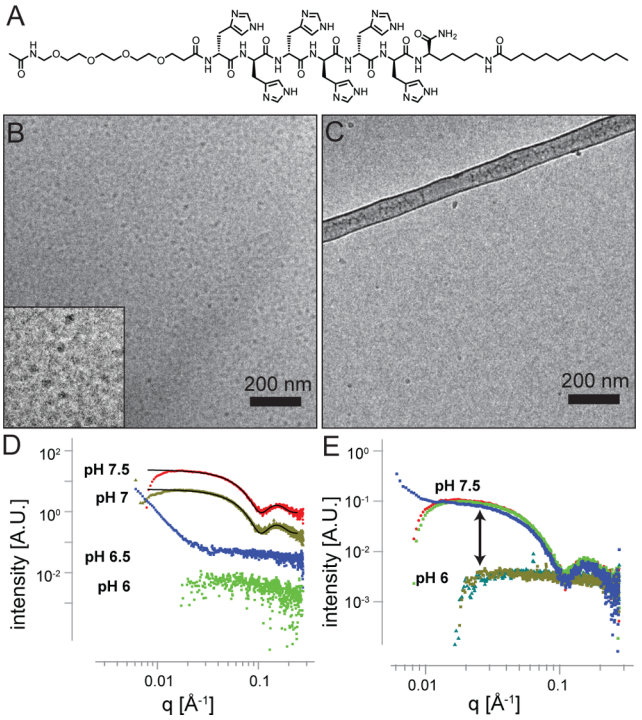

Figure 2. Characterization of OEG-$H_6K(C_{12})$ PA **2**. (A) Structure of PA **2**. (B) Cryo-TEM of PA **2** at pH 7.5 and 5 mM, with an inset to show a zoomed-in image of the spherical micelles. (C) Cryo-TEM of PA **2** at pH 6.0 and 5 mM. (D) SAXS of PA **2** at varying pH, with a core−shell sphere model shown in black. (E) SAXS reversibility studies of PA **2**, where measurements of the same PA solution were taken immediately after each pH change. Each color represents a separate measurement.

morphology was likely related to a combination of steric effects and a peptide sequence with low propensity for β-sheet secondary structure. This strategy was utilized in other previous investigations in our laboratory.[34] The slope of 0 at the low-q range observed in SAXS is indicative of a spherical morphology, and a core−shell sphere fit was performed for PA **2** at pH 7.5 and 7.0. From the SAXS analysis, a shell thickness of 2.8 nm and a core radius of 0.95 nm were determined at both pH 7.5 and 7.0. Unlike the case of the cylinder, there was no observed change in the spherical radius by SAXS, suggesting that protonation of histidine residues abruptly induced nanostructure disassembly. In the case of the PA **1** cylinders at the intermediate range of pH, β-sheet aggregation likely competed with electrostatic repulsion from the histidine residues as suggested in the intermediate SAXS signature at pH 6.5. However, for PA **2** spherical micelles the absence of cohesive forces from β-sheets destabilized the structure upon histidine protonation at pH 6.5 as a result of electrostatic repulsion.

To determine if spherical micelle formation was the result of the β-sheet domain consisting of histidine residues, two new PAs, one with an A_6 (alanine) β-sheet sequence and one with an H_6 sequence, were synthesized and characterized by SAXS (Figure 4S). Both molecules had a similar design to PA **2**, but two lysines were used instead of the OEG because the A_6 sequence was insoluble without including charged residues. The $K_2A_6K(C_{12})$ PA formed nanofibers as indicated by the slope of −1 in the low-q region in SAXS at both pH 7.5 and pH 6.0 (Figure 5S). In contrast, the $K_2H_6K(C_{12})$ PA displayed a slope of 0 in the low-q region, suggesting spheres were present in solution, and this was consistent with SAXS results for PA **2**. Previous studies have shown that the β-sheet propensity for alanine is higher than the propensity of histidine.[35] The SAXS results here suggest that the weaker β-sheet propensity of the histidine domain of PA **2** is essential for spherical micelle formation. We hypothesize that the increased bulkiness between the β-sheet region and the aliphatic tail for PA **2** prevented the formation of β-sheet structures and 1D assemblies. It has been reported that the first amino acid attached to the hydrophobic tail can play a critical role in the morphology of the PA assembly for making long, 1D structures.[36] Similarly, the amide group in PA **2** created a kink between the first amino acid and the aliphatic tail in PA **2**, resulting in a steric barrier that prevented fiber formation. When this amide group was removed using an alternative synthetic procedure, fiber formation was again observed by cryo-TEM (Figure 6S). This PA lacked the steric barrier near the hydrophobic tail but was otherwise similar in chemical structure to PA **2**. These results demonstrate the critical importance of molecular details at the interface of the hydrophobic tail and the peptide sequence in determining supramolecular morphology. Steric hindrance at this interface can be overcome by amino acids such as alanine with a higher β-sheet propensity.

While PA **2** differed morphologically from PA **1**, the pH-sensitive functionality of PA **2** was preserved. Complete and reversible disassembly below pH 6.5 was observed by both cryo-TEM and SAXS (Figure 2C,E), suggesting that the protonation of histidine residues affects morphology in the cases of both spherical micelles and nanofibers. Additionally, buffering by PA **2** was observed with a pK_a of 6.3 by titration, which was slightly higher than that of PA **1** (Figure 2S). Both PAs displayed increased buffering capacities relative to an H_6 peptide, which lacked a hydrophobic tail to promote assembly (Figure 2S). The difference in buffering capacities between the PAs, as revealed by the slope of titration curves near the pK_a, may be due to differences in charge density on the surfaces of the spherical micelles compared to nanofibers. PAs with β-sheet hydrogen bonding in a cylindrical structure generally would have more cohesive forces relative to a sphere without a β-sheet, causing the imidazole protonation to occur at a relatively lower pH for the fiber.[22] Furthermore, the hydrophobic region might be in a more stable configuration for the cylinder due to differences in molecular packing, which could add to its apparent cohesiveness. An additional factor that affects protonation is that the local pH on an assembled PA fiber may also be different compared to bulk solvent.[21]

We observed a pH-dependent decrease in the CD signal for PA **2** (Figure 1S). As expected, PA **2** did not show the characteristic β-sheet signature observed for PA **1**, demonstrating that the β-sheet secondary structure was associated with fiber formation as indicated by SAXS and cryo-TEM.[37] Without the cohesiveness of β-sheet aggregation, the electrostatic repulsion of charged histidine residues in the spherical assemblies easily drives the PAs apart in acidic conditions. Additionally, a significant difference was observed between PAs **1** and **2** in the CAC studies (Figure 3S). With PA **2**, a shift in the λ_{max} of Nile Red was observed only at pH 7.5 and not at pH 6.0, meaning that Nile Red remains in a hydrophilic environment at pH 6.0 for any PA concentration up to 1 mM. While the hydrophobicity of the Nile Red dye might have been able to promote aggregation even at pH 6.0 for PA **1**, the hydrophobic dye was not able to overcome the complete

dx.doi.org/10.1021/ja5042429 | J. Am. Chem. Soc. 2014, 136, 14746−14752

disassembly of PA **2** at the lower pH. These results then suggest that there also might be a difference in hydrophobic interactions between the two PAs, and overall suggests that PA **1** is more cohesive than PA **2**.

Drug Encapsulation and Release. To test these pH-sensitive PAs for their potential as drug delivery systems, camptothecin (CPT) was encapsulated into PAs **1** and **2** using a previously reported 1,1,1,3,3,3-hexafluoro-2-propanol (HFIP) evaporation technique.[30] By dissolving the PA with CPT in HFIP and then reconstituting the solutions in PBS after HFIP evaporation, it was possible to encapsulate CPT into the core of the assembled PA structure with high encapsulation efficiencies (Figure 3A). The encapsulation in the lipid core of the PA is

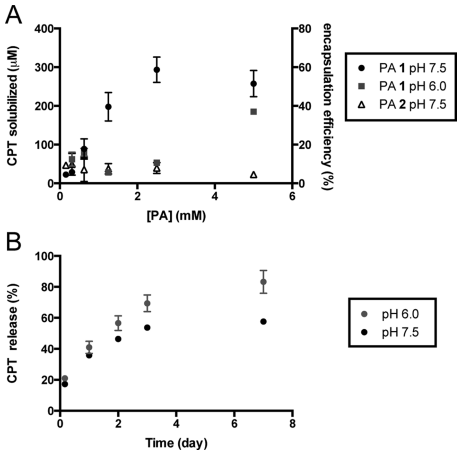

Figure 3. (A) Extent of CPT encapsulation by PA **1** at pH 7.5 and 6.0 and PA **2** at pH 7.5 in PBS with an initial concentration of 500 μM CPT. (B) CPT release rates from PA **1** over 7 days.

primarily driven by the hydrophobicity of CPT. PA **1** at pH 7.5 demonstrated a maximum encapsulation efficiency of approximately 60% at a PA concentration of 2.5 mM, while PA **2** consistently demonstrated poor encapsulation that did not exceed 10% at any measured PA concentration. PA **1** encapsulation efficiency was also measured at pH 6.0. While CPT encapsulation rates were low at PA **1** concentrations of 2.5 mM and below, PA **1** at 5 mM was able to effectively encapsulate CPT at approximately 35% efficiency. These results in conjunction with the CAC studies indicate that the presence of a hydrophobic compound combined with the increased cohesiveness of PA **1** can lead to aggregation and encapsulation by PA **1**, even in acidic conditions. Additionally, the differences between PA **1** and PA **2** suggested that the increased hydrophobic volume of cylindrical structures augments the encapsulation of hydrophobic drugs when compared to spherical micelles of similar chemical composition. With a larger hydrophobic volume, we would expect an increase in entropy of CPT within a cylinder, possibly explaining the increase in encapsulation rates for the cylindrical PA **1** relative to the spherical PA **2.** CPT release studies were conducted on PA **1** into PBS at room temperature at both pH 7.5 and 6.0 (Figure 3B). PA **1** demonstrated significant enhancement in release of CPT at pH 6.0 versus pH 7.5, releasing over 80% of the encapsulated CPT at pH 6.0, while only 50% was released at pH 7.5 by day 7. Because of the low encapsulation efficiency of CPT, we were not able to determine comparable release rates for PA **2**. Based on this strong difference in encapsulation efficiency, the nanofiber-forming PA **1** shows greater capacity as a carrier of hydrophobic cargo than does PA **2**.

Toxicity of PAs Toward Cancer Cells. To determine their effect on cancer cells in physiological and acidic environments, PAs **1** and **2** were tested *in vitro* for toxicity against MDA-MB 231 breast cancer cells (Figure 4). No cytotoxicity was observed

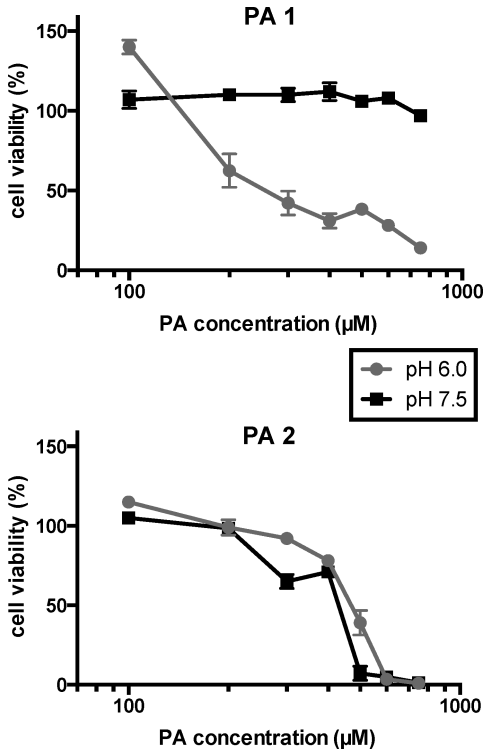

Figure 4. Cytotoxicity of PA nanostructures against MDA-MB-231 breast cancer cells at pH 7.5 and 6.0, measured by MTS assay.

for PA **1** in physiological conditions at pH 7.5, while at pH 6.0 significant cytotoxicity was observed above 100 μM. Conversely, PA **2** exhibited the opposite trend, displaying similar levels of cytotoxicity at pH 6.0 and 7.5 with slightly increased activity at pH 7.5 versus pH 6.0 at concentrations between 300 and 500 μM. At 600 μM PA **2** exhibited significant cytotoxicity at both pH 6.0 and 7.5. The slight increase in toxicity of PA **2** at pH 7.5 as spheres compared to pH 6.0 as soluble monomers showed that toxicity did not correlate with the observed CACs at these pH values. Additionally, the pH-selective cytotoxicity of PA **1** is likely due to a combination of the increased charge of the PA at lower pH and the transition in morphology from fibers to disassembled structures at pH 6. The passage number of the breast cancer cells also appeared to affect their sensitivity to the PAs (Figure 7S). It has been previously reported that cationic PAs can exhibit cytotoxic properties through membrane lysis.[29] It is therefore possible that as the histidines of PA **1** become protonated, they disrupt the cellular membrane of the cancer cells and induce cell death as was observed for other cationic PAs. When in a fiber morphology at pH 7.5, PA **1** did not display the same degree of cytotoxicity when compared to PA **2** at the same pH. This difference could be the result of the morphological difference between the two PAs, suggesting that PA−cell interaction were dependent on supramolecular shape. At higher concentrations, the PAs did not appear to affect cell viability when a cohesive, hydrogen-bonded supramolecular nanostructure formed (PA **1** fiber).

dx.doi.org/10.1021/ja5042429 | J. Am. Chem. Soc. 2014, 136, 14746−14752

***In Vivo* Biodistribution.** To understand the effect of shape and pH-dependent assemblies on tumor accumulation *in vivo*, we compared the biodistribution of spherical and cylindrical assemblies in an orthotopic xenograft model using MDA-MB-231 human breast cancer cells in mice. Because of the poor encapsulation efficiencies of PA 2, we could not compare biodistributions with encapsulated drug. In addition to testing shape dependence in PAs **1** and **2**, we also used the PA OEG-$K_2A_6K(C_{12})$ as a pH-independent control, which assembled into 1D nanostructures at both pH 7.5 and 6.0 by cryo-TEM (Figure 8S). In this case, lysine residues were used as the charged groups to improve the solubility of the PA and to create a cationic PA similar to PAs **1** and **2**. PAs were injected at doses corresponding to limited toxicity as observed by MTS assays both at pH 6 and 7.4 Approximately 5 mol % of PAs **1** and **2** and OEG-K_2A_6 were labeled with AlexaFluor 680 and injected systemically by tail vein. The organ fluorescence intensity was measured *ex vivo* 12 h after injection, and we observed increased tumor uptake in the case of the cylindrical nanostructures compared to spheres (Figure 5A,B). In organs

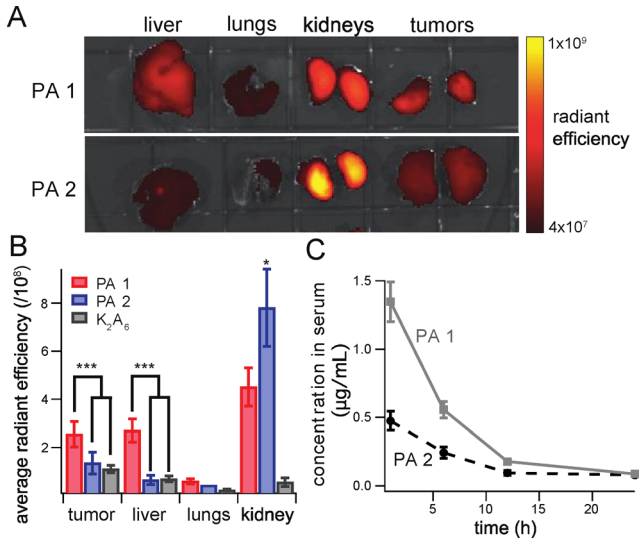

Figure 5. (A) Fluorescent images of biodistribution of AF680-labeled PAs **1** and **2** 12 h after tail vein injection. (B) Quantification of average radiant efficiency for each organ in the PAs **1** and **2** and OEG-$K_2A_6K(C_{12})$ treatment groups (n = 4). (C) Serum fluorescence in mice treated with PAs **1** or **2** at time 0 (n = 4).

that control clearance from the bloodstream, we saw higher levels of fluorescence in the liver for PA **1** and in the kidney for PA **2**, suggesting that the clearance and circulation behavior is strongly dependent on supramolecular morphology. The smaller effective size and increased instability of the spherical micelles likely resulted in enhanced renal filtration, explaining the increased levels of PA **2** observed in the kidney.

The limited renal clearance of PA **1** likely resulted in greater serum concentrations of this PA. Indeed, the fluorescence intensities of PA **1** in serum were greater than those observed for PA **2** at both 1 and 6 h (Figure 5C). A major disadvantage of using self-assembled systems in drug delivery has been poor *in vivo* stability because of disassembly and interactions with serum proteins. Previous studies have demonstrated that covalent cross-linking of micelles improved *in vivo* stability.[38] Analogous to a covalent cross-linking method, the hydrogen bonding present in nanostructures of PA **1** likely imparted improved circulation times. Because the nanofibers were less likely to disassemble in solution, these results suggest that supramolecular cohesion is an important factor in determining circulation behavior, even in the absence of covalent cross-linking.

Importantly, mammary tumor accumulation of PA **1** was greater than that of PA **2** as determined by tumor fluorescence. Furthermore, when comparing fluorescence at 12 and 24 h, a time-dependent decrease in fluorescent intensity was observed for PA **1** in the liver and PA **2** in the kidney (Figure 9S). When compared to the fluorescence of the pH-independent control, OEG-$K_2A_6K(C_{12})$, the fluorescence of PA **1** was greater in the tumor at 12 h, suggesting that the combination of shape and protonation of histidine residues was essential for effective tumor accumulation. The low fluorescent intensities of $K_2A_6K(C_{12})$ suggest that the PA was cleared prior to the time point evaluations, which may have been the result of aggregation after injection. We also used histology sections to examine the distribution of PA within a tumor cross-section. We saw increased fluorescence levels of PA **1** in the tumor tissue relative to both PA **2** and OEG-$K_2A_6K(C_{12})$ (Figure 10S). It was intriguing to find that PA **1** resulted in a punctate pattern of fluorescence in tumor tissues, suggesting that the PA tended to accumulate in certain areas within the tumor environment. The increased cationic charge of PAs **1** and **2** at a lower pH may help increase the drug uptake around the tumor site because of its cationic charge.[39,40] The increased cationic charge of protonated histidines, combined with the cylindrical morphology, likely contributed to PA **1**'s tumor accumulation. Overall, our findings suggest that the supramolecular morphology of nanostructures contributes to tumor uptake with larger cylindrical structures exhibiting enhanced uptake relative to smaller spherical structures likely due to the EPR effect.

■ CONCLUSIONS

We demonstrate here the use of molecular design in peptide amphiphiles to introduce pH sensitivity for reversible self-assembly and also control aggregate morphology. This has been achieved using pH-mediated disassembly due to protonation of histidine residues and also changes in the sites at which hydrophobic segments are attached to peptide sequences. As a result of enhanced supramolecular cohesion, pH-sensitive nanofibers showed greater drug encapsulation and tumor accumulation *in vivo*, validating the need to further explore how delivery system morphology affects the therapeutic efficacy of nanomedicines. This work demonstrates the high level of molecular tunability that is possible in tailoring therapeutic vehicles from these biodegradable nanostructures.

■ ASSOCIATED CONTENT

Ⓢ Supporting Information

Experimental methods, chemical and materials characterization. This material is available free of charge via the Internet at http://pubs.acs.org.

■ AUTHOR INFORMATION

Corresponding Authors

s-stupp@northwestern.edu
vlcryns@medicine.wisc.edu

Author Contributions

[#]These authors contributed equally.

Notes

The authors declare no competing financial interest.

■ ACKNOWLEDGMENTS

This work was supported by the Center of Cancer Nanotechnology Excellence grant 5U54CA151880- 03; National Institutes of Health NIDCR grant 5R01DE015920-09; Department of Defense Breast Cancer Research Program grant W81XWH-10-1-0503 (D.J.T.); Breast Cancer Research Foundation (V.L.C.), and a graduate research fellowship from the National Science Foundation (T.J.M.). The Peptide Core Facility in the Institute for BioNanotechnology and Medicine, Bioimaging Facility (BIF), Cell Imaging Facility (CIF), and Keck Biophysics Facility at Northwestern University were essential for peptide synthesis, cryo-TEM, tumor imaging, and CD, respectively. SAXS results were obtained at the DuPont-Northwestern-Dow Collaborative Access Team (DND-CAT) located at Sector 5 of the Advanced Photon Source (APS). DND-CAT is supported by E.I. DuPont de Nemours & Co., The Dow Chemical Company, and Northwestern University. Use of the APS, an Office of Science User Facility operated for the U.S. Department of Energy (DOE) Office of Science by Argonne National Laboratory, was supported by the U.S. DOE under contract no. DE-AC02- 06CH11357. We thank Dr. C. Newcomb and Dr. L. Palmer for helpful suggestions.

■ REFERENCES

(1) Peer, D.; Karp, J. M.; Hong, S.; FarokHzad, O. C.; Margalit, R.; Langer, R. *Nat. Nanotechnol.* **2007**, *2*, 751.
(2) Davis, M. E.; Chen, Z.; Shin, D. M. *Nat. Rev. Drug Discovery* **2008**, *7*, 771.
(3) Maeda, H.; Matsumura, Y.; Sasamoto, K. *Proc. Am. Assoc. Cancer Res.* **1986**, *27*, 401.
(4) Geng, Y.; Dalhaimer, P.; Cai, S.; Tsai, R.; Tewari, M.; Minko, T.; Discher, D. E. *Nat. Nanotechnol.* **2007**, *2*, 249.
(5) Cai, S.; Vijayan, K.; Cheng, D.; Lima, E. M.; Discher, D. E. *Pharm. Res.* **2007**, *24*, 2099.
(6) Christian, D. A.; Cai, S.; Garbuzenko, O. B.; Harada, T.; Zajac, A. L.; Minko, T.; Discher, D. E. *Mol. Pharmaceutics* **2009**, *6*, 1343.
(7) Gratton, S. E.; Ropp, P. A.; Pohlhaus, P. D.; Luft, J. C.; Madden, V. J.; Napier, M. E.; DeSimone, J. M. *Proc. Natl. Acad. Sci. U. S. A.* **2008**, *105*, 11613.
(8) Wojtkowiak, J. W.; Verduzco, D.; Schramm, K. J.; Gillies, R. J. *Mol. Pharmacol.* **2011**, *6*, 2032.
(9) Tannock, I. F.; Rotin, D. *Cancer Res.* **1989**, *49*, 4373.
(10) Helmlinger, G.; Schell, A.; Dellian, M.; Forbes, N. S.; Jain, R. K. *Clin. Cancer Res.* **2002**, *8*, 1284.
(11) Kale, A. A.; Torchilin, V. P. *Bioconjugate Chem.* **2007**, *18*, 363.
(12) Karve, S.; Bandekar, A.; Ali, M. R.; Sofou, S. *Biomaterials* **2010**, *31*, 4409.
(13) Ulbrich, K.; Etrych, T.; Chytil, P.; Pechar, M.; Jelinkova, M.; Rihova, B. *Int. J. Pharm.* **2004**, *277*, 63.
(14) Chang, G. T.; Li, C.; Lu, W. Y.; Ding, J. D. *Macromol. Biosci.* **2010**, *10*, 1248.
(15) Koo, H.; Lee, H.; Lee, S.; Min, K. H.; Kim, M. S.; Lee, D. S.; Choi, Y.; Kwon, I. C.; Kim, K.; Jeong, S. Y. *Chem. Commun.* **2010**, *46*, 5668.
(16) Gao, Z. G.; Lee, D. H.; Kim, D. I.; Bae, Y. H. *J. Drug Target* **2005**, *13*, 391.
(17) Yin, H. Q.; Lee, E. S.; Kim, D.; Lee, K. H.; Oh, K. T.; Bae, Y. H. *J. Controlled Release* **2008**, *126*, 130.
(18) Lee, E. S.; Oh, K. T.; Kim, D.; Youn, Y. S.; Bae, Y. H. *J. Controlled Release* **2007**, *123*, 19.
(19) Aida, T.; Meijer, E. W.; Stupp, S. I. *Science* **2012**, *335*, 813.
(20) Cui, H.; Webber, M. J.; Stupp, S. I. *Biopolymers* **2010**, *94*, 1.
(21) Matson, J. B.; Newcomb, C. J.; Bitton, R.; Stupp, S. I. *Soft Matter* **2012**, *8*, 3586.
(22) Ghosh, A.; Haverick, M.; Stump, K.; Yang, X. Y.; Tweedle, M. F.; Goldberger, J. E. *J. Am. Chem. Soc.* **2012**, *134*, 3647.
(23) Trent, A.; Marullo, R.; Lin, B.; Black, M.; Tirrell, M. *Soft Matter* **2011**, *7*, 9572.
(24) Kokkoli, E.; Mardilovich, A.; Wedekind, A.; Rexeisen, E. L.; Garg, A.; Craig, J. A. *Soft Matter* **2006**, *2*, 1015.
(25) Hartgerink, J. D.; Beniash, E.; Stupp, S. I. *Proc. Natl. Acad. Sci. U. S. A.* **2002**, *99*, 5133.
(26) Velichko, Y. S.; Stupp, S. I.; de la Cruz, M. O. *J. Phys. Chem. B* **2008**, *112*, 2326.
(27) Ortony, J. H.; Newcomb, C. J.; Matson, J. B.; Palmer, L. C.; Doan, P. E.; Hoffman, B. M.; Stupp, S. I. *Nat. Mater.* **2014**, in press.
(28) Lin, B. F.; Megley, K. A.; Viswanathan, N.; Krogstad, D. V.; Drews, L. B.; Kade, M. J.; Qian, Y. C.; Tirrell, M. V. *J. Mater. Chem.* **2012**, *22*, 19447.
(29) Standley, S. M.; Toft, D. J.; Cheng, H.; Soukasene, S.; Chen, J.; Raja, S. M.; Band, V.; Band, H.; Cryns, V. L.; Stupp, S. I. *Cancer Res.* **2010**, *70*, 3020.
(30) Soukasene, S.; Toft, D. J.; Moyer, T. J.; Lu, H.; Lee, H. K.; Standley, S. M.; Cryns, V. L.; Stupp, S. I. *ACS Nano* **2011**, *5*, 9113.
(31) Webber, M. J.; Newcomb, C. J.; Bitton, R.; Stupp, S. I. *Soft Matter* **2011**, *7*, 9665.
(32) Minkenberg, C. B.; Li, F.; van Rijn, P.; Florusse, L.; Boekhoven, J.; Stuart, M. C.; Koper, G. J.; Eelkema, R.; van Esch, J. H. *Angew. Chem., Int. Ed.* **2011**, *123*, 3483.
(33) Lee, H. K.; Soukasene, S.; Jiang, H. Z.; Zhang, S. M.; Feng, W. C.; Stupp, S. I. *Soft Matter* **2008**, *4*, 962.
(34) Muraoka, T.; Koh, C. Y.; Cui, H.; Stupp, S. I. *Angew. Chem., Int. Ed.* **2009**, *121*, 6060.
(35) Pawar, A. P.; Dubay, K. F.; Zurdo, J.; Chiti, F.; Vendruscolo, M.; Dobson, C. M. *J. Mol. Biol.* **2005**, *350*, 379.
(36) Paramonov, S. E.; Jun, H. W.; Hartgerink, J. D. *J. Am. Chem. Soc.* **2006**, *128*, 7291.
(37) Pashuck, E. T.; Cui, H.; Stupp, S. I. *J. Am. Chem. Soc.* **2010**, *132*, 6041.
(38) Li, Y.; Xiao, W.; Xiao, K.; Berti, L.; Luo, J.; Tseng, H. P.; Fung, G.; Lam, K. S. *Angew. Chem., Int. Ed.* **2012**, *124*, 2918.
(39) Yim, H.; Park, S. J.; Bae, Y. H.; Na, K. *Biomaterials* **2013**, *34*, 7674.
(40) Stylianopoulos, T.; Soteriou, K.; Fukumura, D.; Jain, R. K. *Ann. Biomed. Eng.* **2013**, *41*, 68.